Insights into the flow and scalar structures when shifting from methane to hydrogen turbulent flames using simultaneous PIV – OH PLIF and spontaneous Raman scattering

Kuppuraj Rajamanickam, Ariff Magdoom Mahuthannan, Corine Lacour, Said Idlahcen, Armelle Cessou, David Honoré, Bertrand Lecordier

Proceedings of the Combustion Institute 40 (2024) 105708

Contents lists available at ScienceDirect

Proceedings of the Combustion Institute

journal homepage: www.elsevier.com/locate/proci

Insights into the flow and scalar structures when shifting from methane to hydrogen turbulent flames using simultaneous PIV – OH PLIF and spontaneous Raman scattering

Kuppuraj Rajamanickam [a,b,1,*], Ariff Magdoom Mahuthannan [c,1], Corine Lacour [a], Said Idlahcen [a], Armelle Cessou [a], David Honoré [a], Bertrand Lecordier [a]

[a] INSA Rouen Normandie, Univ Rouen Normandie, CNRS, Normandie Univ, CORIA UMR 6614, F-76000 Rouen, France
[b] Department of Mechanical Engineering, Imperial College London, Exhibition Rd, London SW7 2AZ, United Kingdom
[c] Ohio State University, 281 W Lane Ave, Columbus, OH 43210, United States

ARTICLE INFO

Keywords:
Hydrogen combustion
Bluff body burner
Spontaneous Raman scattering (SRS)
OH-PLIF
PIV

ABSTRACT

This study discusses fundamental turbulence-chemistry interactions in a canonical non-premixed bluff body burner fueled with 100% methane or hydrogen. Simultaneous time-resolved PIV&OH-PLIF and 1D Spontaneous Raman Scattering (SRS) have been employed to provide deeper insights into the difference in combustion regimes between CH_4 and H_2 operations. The analysis of the instantaneous time-resolved PIV and OH-PLIF datasets reveals the presence and absence of local extinctions in methane and hydrogen flames despite the mean flow topology being similar across the test cases. The instantaneous scatter plots of 1D Raman data in the mixture fraction space further quantified the spatial evolution of temperature and major species. Finally, the regime identification scheme is implemented over instantaneous 1D SRS data to identify the different flame/mixture regimes. The change in combustion regime is observed even very close to the burner exit while switching between CH_4 and H_2, which is attributed to the probability of localized flame extinctions. Overall, this study provides detailed interlinks between flow field aerodynamics and scalar structures in the two different flames whose thermo physical properties are entirely different and form a comprehensive database for cornerstone computational model validation.

1. Introduction

Hydrogen combustion is crucial in decarbonizing energy-intensive industries (e.g., brick, steel manufacturing)[1]. Industries are targeting progressively increasing the hydrogen blend in the current natural gas-fired burners. Although hydrogen (H_2) is a promising fuel for decarbonization, the differences in the fundamental parameters like flame speed and extinction strain rate cause technological challenges in operating the burner at high hydrogen enrichment levels [2].

Bluff body stabilized non–premixed burners are widely used in energy-intensive industrial applications. Most of the available literature on H_2 addition in bluff body stabilized non–premixed burners is focused on the design optimization and characterization of NOx emissions. Moreover, only a few studies reported the operating characteristics of a burner at 100% H_2. The bluff body burner's complex flow structures (e.g., recirculation zone) mandate a detailed fundamental understanding of turbulence-chemistry interactions. To bridge this gap, we have conducted an experimental investigation on a canonical non-premixed bluff body burner operated with 100% CH_4 and 100% H_2. High-fidelity laser-based diagnostic measurements (1. Simultaneous time-resolved PIV & OH-PLIF 2. Spontaneous Raman Scattering) are implemented to unravel the fundamental turbulence-chemistry interactions and their changes from CH_4 to H_2 use.

2. Experimental setup

A canonical non-premixed bluff body burner is used in this study. The schematic of the burner is shown in Fig. 1. Fuel is injected through the central hole with a diameter (D_f) of 6 mm, and the annular passage ($D_b = 24$ mm, $D_a = 26$ mm) is used for the air stream. A fuel injection

* Corresponding author.
E-mail address: k.rajamanickam@imperial.ac.uk (K. Rajamanickam).
[1] K. Rajamanickam and A.M. Mahuthannan equally contributed to this work.

https://doi.org/10.1016/j.proci.2024.105708
Received 4 December 2023; Accepted 20 July 2024
Available online 22 August 2024

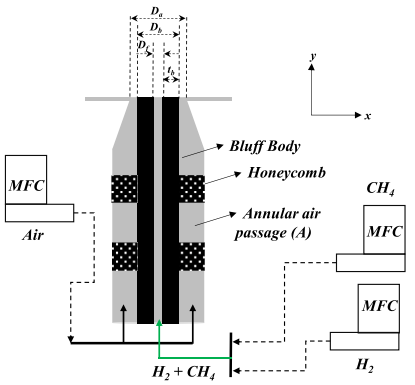

Fig. 1. Configuration of the canonical non-premixed bluff-body burner [3].

pipe's thickness ($t_b = 9\ mm$) acts as a cylindrical bluff body, creating a recirculation zone just above the burner exit. Mass flow controllers (Bronkhorst) are used to control both air and fuel flow rates. Two test cases are considered, one with 100 % methane and the other with 100 % hydrogen. The operating conditions are listed in Table 1. In both the test cases, the thermal power and annular air flow rate have been maintained constant, allowing us to compare the flow-flame interactions under relatively similar aerodynamics.

3. Laser Diagnostic Techniques

3.1. PIV and OH–PLIF measurements

The velocity field and OH fluorescence have been measured simultaneously using time-resolved PIV & OH-PLIF systems at 5 kHz. For each test case, 10000 images are acquired, corresponding to the acquisition time of 2 seconds. The integral time scale calculated from the instantaneous velocity field (particularly in the region where RMS is highly pronounced) is approximately 5 – 10 ms. Hence, the chosen acquisition time of 2 seconds is sufficient. Moreover, as confirmed by the proper orthogonal decomposition (POD) and 1D continuous wavelet transform (1D-CWT) analysis shown in our previous work [3], the most dominant frequencies are in the range of 10 - 400 Hz; hence, the chosen sampling rate of 5 kHz is well enough to resolve the fluctuations in the flow.

The details concerning the hardware (e.g., laser, camera, spectral filters) and PIV post-processing can be found in [3].

3.2. 1D Spontaneous Raman Scattering (SRS)

The schematic of the in-house developed SRS system is presented in Fig. 2. A second harmonic of the Nd: YAG laser with a 10 Hz repetition rate is utilized. The laser power is ~1.8 J/pulse (pulse duration – 1000 ns) at 532 nm. A half-wave plate is used at the laser exit to optimize the Raman scattering in the collection direction. The laser is focused on the probe volume using a spherical lens (L1) with a focal length (f) of 1000 mm. An achromatic lens (L2; f=150 mm) is employed in the orthogonal direction to collect the Raman signal. A second achromatic lens (L3) is used to focus the signal onto a 400 μm slit (S), which acts as the spatial filter to cut down the excessive flame emissions. Following the slit, another spherical lens (L4; f=200 mm) is used to collimate the collected signal, sending it through an electro-optical shutter (EOS). The EOS consists of a vertical polarizer, a Pockels cell, and a horizontal polarizer. It is used to transmit the Raman signal during a short duration synchronously to the laser pulse (1 μs), thereby limiting the CCD exposure to flame emission during the readout time. After the EOS, the Raman scattering signal is focused on the spectrometer's entrance using a spherical lens (L5; f=300 mm). A notch filter (532 nm) is placed before L5.

Table 1
Operating conditions

Fuel	Re_{fuel}	Re_{air}	*Power (kW)*	$MR = \left(\frac{\rho_{air} U_{air}^2}{\rho_f U_f^2}\right)$
CH_4	4370	10575	16.8	0.25
H_2	2250	10575	16.8	0.21

The spectrometer (Princeton Instruments, IsoPlane SCT 320) is coupled with an eMCCD camera (PIXIS 400). The eMCCD resolution is 1340 pixels in the horizontal direction and is dedicated to capturing spectral information from 567 nm to 694 nm. The 400 pixels are divided into eight regions of interest (ROIs) in the vertical direction, yielding a probe length (L) of 3.44 mm. However, only the six central ROIs are used due to lower signal in the edge ROIs, resulting in an effective total probe length of 2.58 mm. The effective spatial resolution is approximately 430 μm for each ROI.

The selected spectral range from 567 nm to 694 nm can capture Raman shifts of O_2, N_2, CH_4, H_2, CO, CO_2, and H_2O simultaneously when excited using 532 nm. The burner is mounted on a motorized bench and moved in 2 mm steps, covering x = -6 mm to 30 mm in the radial direction. At each traverse location, 1000 instantaneous shots are recorded. Furthermore, measurements are carried out at six (y = 5, 10, 20, 35, 45, 60 mm) axial heights above the burner (HAB).

An in-house Raman post-processing tool [4] adapting the 'spectral fitting' method is employed. Unlike traditional approaches (e.g., calibration methods), the spectral fitting process can be directly applied to the normalized spectra, enabling the computation of absolute temperature without calibration. More details on the working, accuracy, and precision of the Raman post-processing tool have been included in the supplementary material.

4. Overall flow and flame structures

4.1. Mean flow field

The time-averaged and RMS profiles of the two test cases are shown in Fig. 3. The flow field features three distinct zones, namely, Recirculation Zone (RZ), Neck Zone (NZ), and Jet-like flame zone (JZ). The presence of RZ leads to two inner shear layers (ISL1, ISL2) in the flow field. As the annular air flow converges towards the central fuel jet in the neck zone (NZ), causing the merging of ISL1 with ISL2, the flow behaves as simple coaxial jet flows above the RZ. It is interesting to note that, despite a significant rise in the central fuel jet velocity (U_f) from 12 m/s to 35 m/s (marked with a blue dashed rectangle) between CH_4 and H_2 cases, the global topology of the mean flow field is relatively similar across both test cases. The hydrogen density is much lower than the methane, which keeps the momentum ratio (MR) relatively the same between CH_4 and H_2 (Table 1). This feature eventually leads to a similar mean flow topology for CH_4 and H_2. However, both V_{rms} and U_{rms}, profiles showed a substantial difference between CH_4 and H_2. For the CH_4 case, the RMS is more pronounced in the neck zone (NZ) due to the strong interaction between the central fuel and the annular air jet.

On the other hand, both V_{rms} and U_{rms} show strong fluctuations in the central fuel jet region for the H_2. In line with the observations of [6,7], the reduction in the central fuel jet Reynolds number (Re_{fuel}) due to the low density associated with the H_2 case, which causes the jet to become globally unstable and exhibit intermittent oscillations. We recommend the readers see videoS1 in the supplementary file to visualize this phenomenon.

4.2. Mean OH, Temperature, and Mixture Fraction Profiles

The superimposed mean flow field and OH contours (Fig. 4 a) from combined PIV & OH-PLIF and the radial profiles of mean temperature (T) and mixture fraction (ξ) (Fig. 4b) obtained from SRS measurements

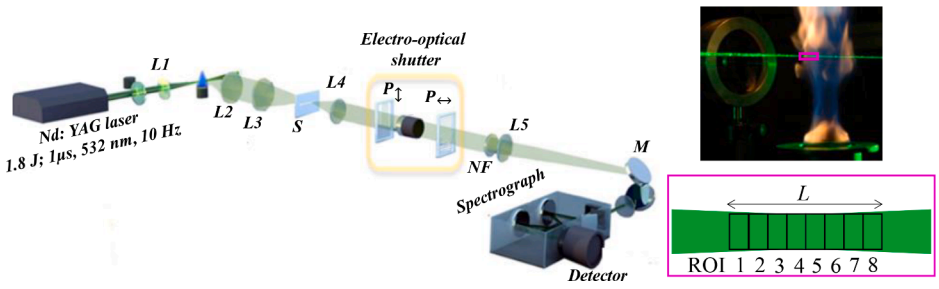

Fig. 2. Schematic of Spontaneous Raman Scattering (SRS) setup
(L1 = 1000 mm; L2 = 150 mm; L3 =300 mm; L4=200 mm; L5-300 mm; S-slit; NF-Notch Filter; M-Mirror) [5].

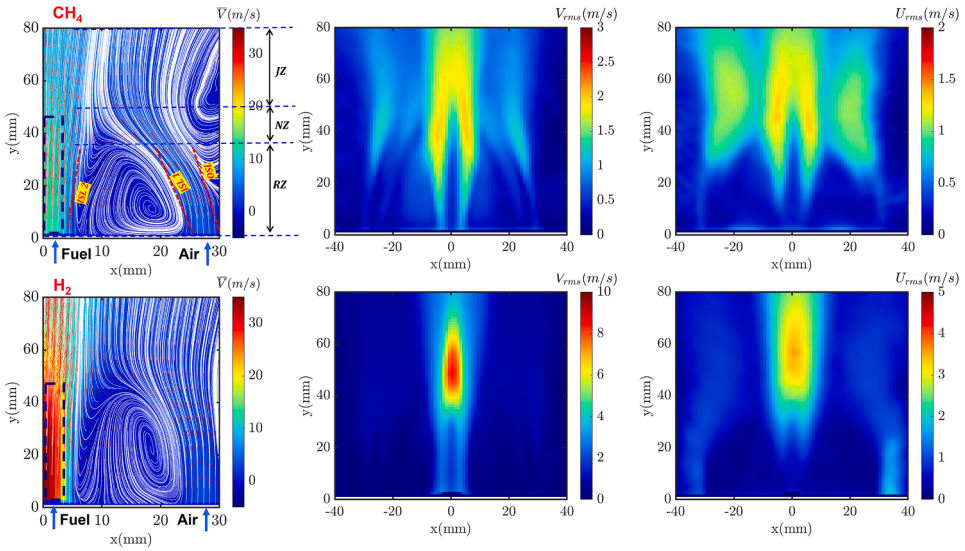

Fig. 3. Time-averaged flow field and V_{rms}, U_{rms} contours; [RZ, NZ, JZ – Recirculation, Neck, Jet Zones].

across the different axial heights above the burner are compared for CH_4 and H_2. Mixture fraction (ξ) is calculated based on the major species concentration using Bilger's formulation (Equation 1).

Where 'Y' represents elemental mass fractions of Carbon (C), Oxygen (O), and Hydrogen (H); 'W' represents atomic weights. The subscripts F and Ox denote fuel and oxidizer streams, respectively. Despite similar mean flow topology, the mean OH intensity profiles of CH_4 and H_2 are considerably different (Fig. 4a). In the case of methane, the OH intensity is predominantly found only in the RZ. In contrast, OH intensity is distributed across all the zones for H_2. The mean temperature profiles from SRS measurements further confirm this observation. For instance, at y = 45, 60 mm, the peak value of T_{mean} for CH_4 is much lower than the H_2 case (Fig. 4b pointed with black arrows).

Furthermore, despite the PLIF image showing the significant presence of OH within the RZ in both cases, the SRS measurements show a lower T_{mean} for CH_4 than H_2 (see Fig. 4b; Y = 10 mm, 20 mm). The physical mechanisms concerning differences in the mean OH and temperature profile between the H_2 and CH_4 flames across the different HABs will be explained in upcoming sections.

$$\xi = \frac{\frac{2\left(Y_c - Y_{c,Ox}\right)}{W_c} + \frac{\left(Y_H - Y_{H,Ox}\right)}{2W_H} - \frac{\left(Y_O - Y_{O,Ox}\right)}{W_O}}{\frac{2\left(Y_{c,F} - Y_{c,Ox}\right)}{W_c} + \frac{\left(Y_{H,F} - Y_{H,Ox}\right)}{2W_H} - \frac{\left(Y_{O,F} - Y_{O,Ox}\right)}{W_O}} \quad (1)$$

The mean mixture fraction (ξ_{mean}) profile (Fig. 4b) at the fuel jet location (-6 < x < 6 mm) is nearly identical for both the test cases till the axial locations of Y ≤ 20 mm. Moreover, the value of $\xi_{mean} = 1$ within the central fuel jet region, indicating the potential core and ξ_{rms} is mainly aligned with the fuel jet's shear layer (i.e., ISL 2). However, in the RZ (6 < x <20mm), CH_4 shows slightly higher values than H_2 (reasons explained in later sections). At higher axial locations (i.e., y ≥ 35 mm), a reduction in the peak value and width of the ξ_{mean} profile is noticed for H_2 (marked with green arrows in Fig. 4b). This is attributed to the higher probability of flame presence in the case of H_2, as confirmed by the mean OH intensity and T_{mean} (Fig. 4a, b; H_2). Moreover, the intermittency observed in the H_2 fuel jet further led to an increase in the ξ_{rms} (solid black line on Fig. 4b; y > 35 mm). This trend is matching well with the V_{RMS}, U_{RMS} contours of H_2 shown in Fig. 3 (bottom row).

5. Insights from simultaneous time-resolved PIV & OH-PLIF

The previous section highlighted the difference in the mean flame structures between CH_4 and H_2. The instantaneous data sets are presented in this section to provide further insights. Fig. 5 illustrates the superimposed strain field (κ_{hyd}) and flame contours obtained from simultaneous time-resolved PIV, OH-PLIF. In the chosen canonical burner configuration, it is known from previous studies[8,9] that hydrocarbon flame (e.g., CH_4 flame) undergoes local extinction in NZ. This is because, in the NZ, the flame strongly interacts with flow-induced strain (κ_{hyd}) in the central fuel jet, whose values are often much higher than the flame extinction strain rate (κ_{ext}), leading to the local extinction of the flame fronts. A similar phenomenon is observed in the test case of CH_4 (Fig. 5). For instance, at t = 0 ms, flame interacts with the strong strain field in the central fuel jet and eventually undergoes local extinction at t = 0.2 ms. Subsequently, as shown in the t = 0.8, 1.2 ms, the upper branch convected downstream by shedding vortices in OSL, leading to the failure of reconnection with the lower branch (also

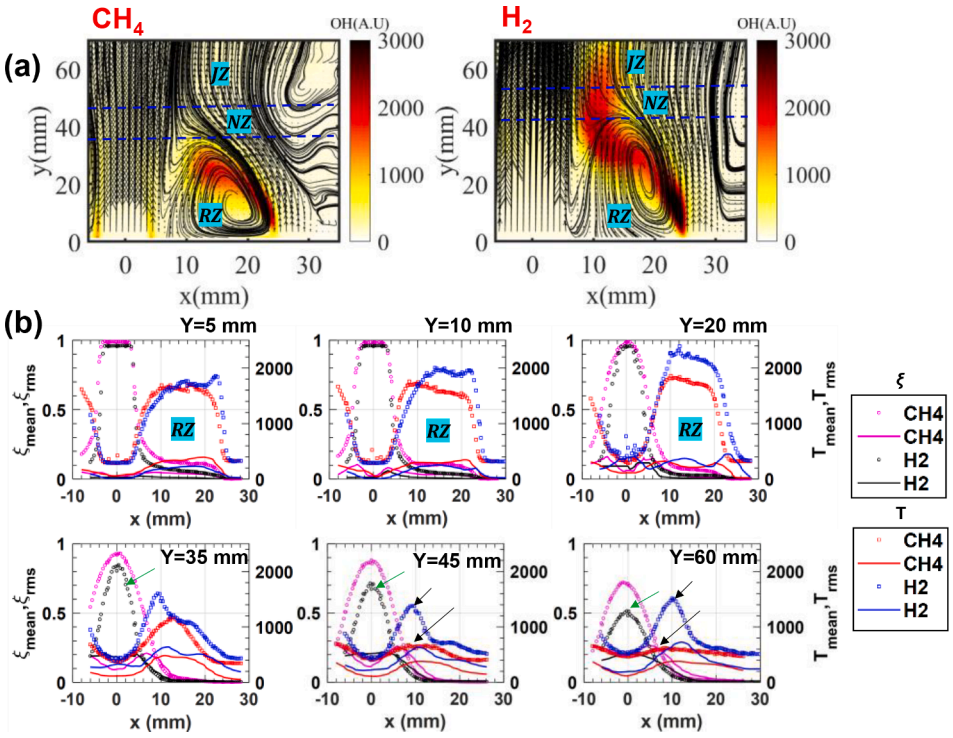

Fig. 4. (a) Illustration of the superimposed mean flow field and OH profile; (b) Radial profiles of time-averaged mixture fraction (ξ) and temperature (T) (the circle and the dashed line denote mean, RMS quantities).

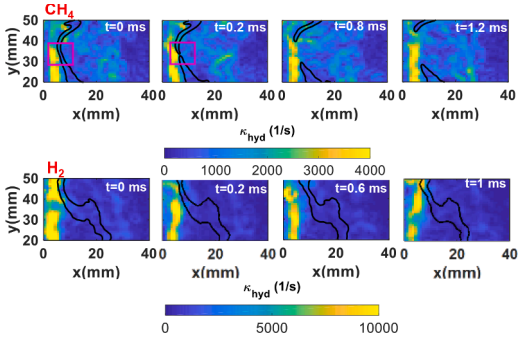

Fig. 5. Instantaneous strain field and OH-PLIF contours

see video S3). As a result, the lower branch stabilized in the RZ acts as a pilot in the reignition of the fresh reactants, thereby establishing the stable flame. As highlighted in our previous study [3], the time delay between the reignition and re-establishment of stable flame is quite long for the CH_4 case, resulting in the flame's presence predominantly in the RZ. This is why the mean OH structure appeared mainly within RZ for the CH_4 flame (Fig. 4a) and also a drastic reduction in mean temperature (T_{mean}) above the RZ (i.e., y $\geq$ 35 mm in Fig. 4b; CH_4). Furthermore, flame exhibits intermittent lift-off inside the RZ, following the local extinctions (see Video S5), which eventually led to a decrease in T_{mean} at Y = 5, 10, 20 mm (Fig. 4b; CH_4).

On the other hand, local extinction is not witnessed with H_2 despite strong flame front interaction with the larger strain magnitude value in the central fuel jet (see video S4). This is due to the significant rise in the flame extinction strain rate (κ_{ext}) in the pure hydrogen flames. The absence of local extinction led to the higher OH intensity distribution across all three zones (RZ, NZ, JZ-Fig. 4a; H_2) and, subsequently, higher T_{mean} in the downstream locations (i.e., y $\geq$ 35 mm in b; H_2).

6. Instantaneous scatter plots

Fig. 6 compares the instantaneous temperature (T) and O2 mass fraction (YO2) scatter plots in mixture fraction space. For brevity, only two axial heights representing the near (y = 5mm) and far (y = 60 mm) fields are shown.

The solid blue line on the temperature scatter plots indicates the stoichiometric mixture fraction (ξ_{st}) value, and the data points are color-coded based on the radial locations. At y = 5mm, the presence of RZ leads to high-temperature data points distributed over the broader radial region of x = 6 – 24 mm (see green, black, and red color dots on T scatter plots at y = 5mm). Interestingly, for methane, at y = 5mm, the temperature samples are dispersed between 500 K and 2000 K in the x = 18 – 24 mm region (Fig. 6; red color dots on CH_4; y = 5mm plot) despite the flame being predominantly located in this region as conformed from the mean OH image (Fig. 4a). As shown in video S5, the CH_4 flame exhibits intermittent lift-off at y = 5 mm, resulting in temperature distribution between higher and lower values. The increase in O_2 mass fraction (Fig. 6; see Y_{O2} in CH_4; y = 5mm) at this location confirms the presence of an unburnt mixture. Additionally, the intermittent lift-off leads to an increase in ξ_{mean}, T_{RMS} at y= 5mm for the case of CH_4 (Fig. 4b; y = 5mm).

Next, at y = 60 mm, the temperature scatter plot of the CH_4 flame reveals a lot of samples featuring low-temperature values near the stoichiometric mixture fraction, confirming the least probability of flame presence due to failure of reconnection of broken flame branches [3]. On the other hand, the absence of local extinctions in the H_2 flames causes the samples to stay at a high temperature. Furthermore, at this height, the flame is located near the central fuel jet region; therefore, the high-temperature samples are observed at x = 6 – 12 mm (see green color; y = 60 mm; H_2). Overall, Fig. 6 clearly delineates different regimes, for example, a broader scatterplot at high temperatures (see temperature scatter plot of CH4 case at y = 5 mm) showing diffusion flame with oxygen mixing to the stoichiometric composition, premixed regime and non-reactive mixture due to local extinction (especially in the methane case; see y = 60 mm; CH_4). These different regimes appear within the mixture fraction frame. The following section explains how to

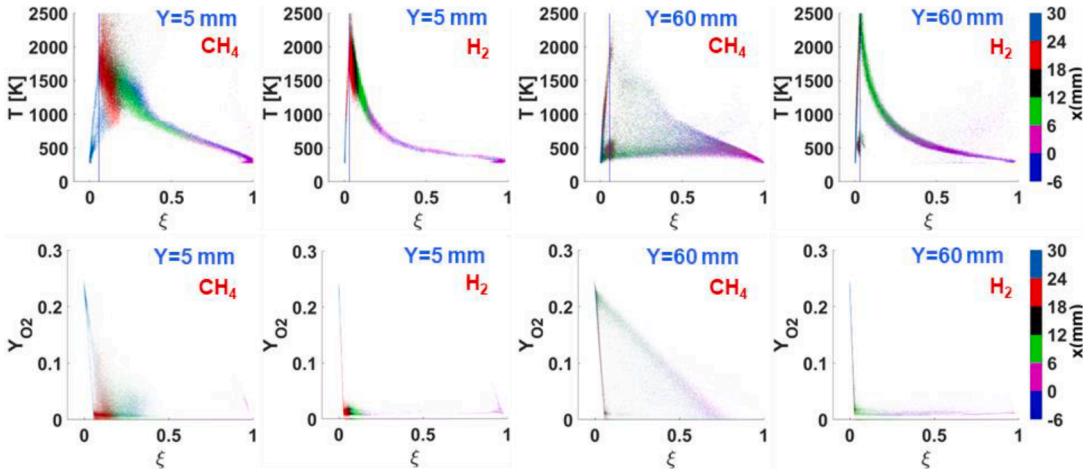

Fig. 6. Instantaneous scatter plots of temperature (T) and oxygen mass fraction (Y_{O2}) in mixture fraction space

identify these regimes across the flame.

7. Flame/mixture regimes

To map the different flame/mixture regimes, we first identified the nature of the fuel and oxidizer mixing (e.g., diffusion, premixed) at each radial location based on the criteria proposed by Takneno [10].

$$FR = \frac{\nabla Y_F . \nabla Y_{ox}}{|\nabla Y_F . \nabla Y_{ox}|} \tag{2}$$

Then, the identified state of the mixture is further classified into lean and rich by comparing the difference between local and stoichiometric mixture fractions. This approach slightly differs from the modified flame index proposed by [11], which is applied only in the active flame regions. However, our interest is in the spatial mapping of the premixed, fuel, and air-side diffusion flame/mixture regimes. Therefore, we have applied regime identification across all the radial positions to determine the regime of possible combustion. The gradient-based approach is chosen instead of gradient-free methods [12,13], as the former involves a less complicated computational procedure.

The classification of different flame regimes is illustrated in Fig. 7. First, the gradients of fuel and oxidizer are estimated from instantaneous Raman data. For example, Fig. 7 shows the fuel and oxidizer gradients computed at y = 5 mm in the H_2 case. In the second step, the threshold value of 600 K is applied to mask the no-flame (NF) region, as marked with yellow and blue boxes (Fig. 7), usually located in the fuel (NFF) and annular air jet (NFA) region. Next, the region where the two gradients are weak is tagged as the lean or rich premixed regime (see LPR/RPR in Fig. 7). RZ generally exhibits such behavior where the fuel and oxidizer gradients are weak. Here, the difference in local (ξ) and stoichiometric (ξ_{st}) mixture fraction values determine lean (LPR-cyan color) or rich premixed (RPR-black color) regimes. Finally, the region where one

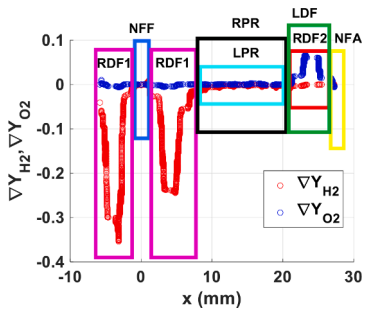

Fig. 7. Steps involved in flame regime identification.

gradient is very strong and the other is weak represents diffusion flame (DF)/mixture. The DF is classified into fuel (RDF) and air (LDF) sides based on the relative difference between ξ and ξ_{st}. Interestingly, RDF is identified in some instances even on the air side; hence, RDF is further classified into RDF1 and RDF2, representing the air and fuel sides.

It should be noted that smoothening has been applied to the computed gradients to remove the outliers before implementing the above-described regime identification algorithm. Such smoothening does not influence the results, as we are not interested in the absolute value of the gradients. Fig. 8 represents normalized counts of different regimes obtained at each radial location.

7.1. Recirculation zone (0 < y < 35 mm)

Interestingly, in the CH_4 case, at ISL1 (see the red dashed box in Fig. 8; y = 5 mm; CH4), the dominance of the RDF1 regime is witnessed despite the flame being located at the air side. This is attributed to the intermittent lift-off (video S5) leading to the accumulation of an unburnt mixture and, thereby, a rich diffusion mixture regime. On the other hand, the absence of lift-off in the H_2 resulted in the dominance of LDF. Next, in both the CH_4 and H_2 cases, the RZ (~ x = 10 -22 mm; marked with a blue color box in Fig. 8) exhibits rich premixed (RPR) behavior; the mechanisms causing this will be explained later in this section. As shown in the instantaneous OH-PLIF image (see the green color box in Fig. 9; CH_4), a small pilot flame is witnessed at ISL2 in the case of CH_4, whereas no such flame is seen in H_2. On the contrary, the RDF1 (pink color bars marked with green dashed box; Fig. 8; y = 5 mm) is identified in the region close to the central fuel jet (i.e., ISL2) in both cases.

This can be explained as follows: local extinctions observed in the CH_4 flame causes the O_2 to reach ISL2 from ISL1 (see pink arrows in Fig. 9a; CH_4), establishing the pilot flame (marked with a green box). However, for the H_2 case, the active flame presence (Fig. 9b; H_2) relatively consumed all available O_2 at ISL1, leading to no pilot flame at ISL2. Henceforth, the obtained RDF1 represents the actual flame in CH_4, whereas, for H_2, it just means a high-temperature region without the flame being active. Therefore, as explained in Section 7, the DF doesn't necessarily mean the physical presence of actual diffusion flame; rather, it represents the mixture that potentially favors the diffusion flame in that region.

Despite fresh air entering the RZ following the local extinction, the RZ of CH_4 exhibits RPR instead of LPR behavior because of the unburnt mixture induced by intermittent flame lift-off. However, in the H_2 case, the active flame at ISL1 limits the oxygen's presence inside the RZ, leading to RPR. Hence, the mechanism that governs the formation of RPR inside RZ between CH_4 and H_2 are entirely different. The results obtained at y = 10, 20 mm show relatively similar behavior to y = 5 mm,

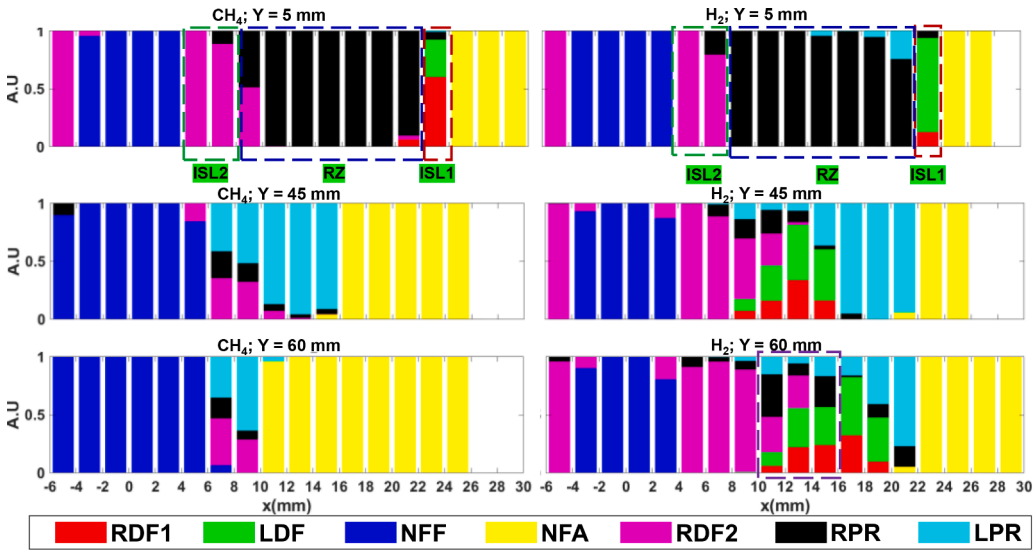

Fig. 8. Normalized counts of flame regime maps across different radial and axial locations.

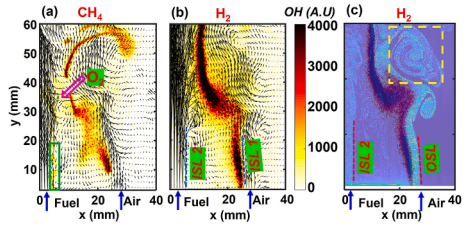

Fig. 9. a,b Instantaneous snapshots of the superimposed flow field and raw OH contours; c – superimposed PIV and OH-PLIF raw images

except inside the RZ, the combination of LPR and RPR is witnessed (regime plots not shown here) because of the more annular air entering the neck zone.

7.2. Neck and Jet Zones (y> 35 mm)

Interestingly, the premixed regime (see LPR in y >35 mm; Fig. 8; CH_4, H_2) remains beyond RZ. As shown in Fig. 9c (yellow dashed box), coherent shedding vortices in this region induce a premixed regime in the OSL. This region is dominated by annular air, leading to the LPR regime. The change in the flame location from ISL1 to ISL2 leads to the inward radial shift in the RDF1, RDF2, and LDF flame regimes. As in the neck and jet zones, the probability of active flame for CH_4 is very low due to local extinction, which leads to a progressive increase in the distribution of no flame region (NFA) with increasing axial heights. It is worth mentioning that, unlike near field (i.e., RZ), the RDF2 in H_2 at these axial heights represents actual flame, as evidenced by Fig. 9b (H_2). Noticeably, the RDF1 and LDF flame regimes are again shifted radially outward for H_2 at y =60 mm. The radial flame flapping (see video S2) triggered by intermittently oscillating central fuel jet induces this phenomenon.

Furthermore, it is worth noting that in the far field, several combustion regimes coexist at a particular radial location, for example, at y = 60 mm; x = 10 -16 mm (see purple dotted box in H_2; y =60 mm), the flame intermittently switches between the lean premixed (LP), air (LDF) and fuel side (RDF1, RDF2) regimes. Strong flame flapping (Video S2) and large-scale shedding vortices (Fig. 9c) in the OSL led to multiple combustion regimes.

8. Conclusion

Simultaneous time-resolved PIV&OH-PLIF and 1D SRS measurements have been implemented in the canonical non-premixed bluff body burner operated with 100% methane or 100% hydrogen. The thermal output of the burner and annular air flow rate is maintained constant across the test cases to keep the near-field aerodynamics relatively the same. Despite the similar mean flow topology, OH-PLIF results reveal the change in mean flame structure attributed to the presence and absence of localized flame extinctions in CH_4 and H_2 flames. The 1D SRS results examined in mixture fraction space further confirmed this observation. A modified flame index approach is used to identify the different flame regimes from SRS data, linking their evolution with varying flame conditions. The change in fuel highlights the switching of combustion mode even very close to the burner exit. For instance, the intermittent flame lift-off close to the burner exit (y=5mm) of the CH_4 flame causes the dominance of rich diffusion flame. At the same location, it is transitioned to a lean diffusion flame regime in the H_2 case. This study provides detailed interlinks between flow-turbulence interaction concerning pure methane and hydrogen flames and forms a comprehensive database for cornerstone computational model validation.

Novelty and significance statement

This work provides detailed novel insights into the turbulence-chemistry interactions in switching between the 100% methane and 100% hydrogen flames at constant thermal power. Tests have been carried out in a canonical configuration of a non-premixed bluff body burner mimicking the geometry typically used in energy-intensive industries (e.g., brick and steel manufacturing and utility boilers). High-fidelity laser diagnostic tools (1D Spontaneous Raman scattering and simultaneous time-resolved PIV, OH-PLIF) have been employed to provide a detailed database including temperature, major species concentrations and their gradients, high-speed simultaneous velocity and burnt gas fields. The combined diagnostics revealed detailed interlinks between flow field aerodynamics and scalar structures in flames generated from the fuels (CH_4 and H_2) whose thermo physical properties are entirely different. Furthermore, the dataset on 100% hydrogen turbulent flame in the canonical burner configuration associated with the CH4 ones will create significance in the computational model validation.

Author contributions

K. Rajamanickam – Conceptualization, Investigation, Data Analysis, Writing – Original Draft; **A.M. Mahuthannan** – Conceptualization, Investigation, Data Analysis, Writing – Original Draft; **C. Lacour** – Validation, Supervision, Writing – Review & Editing; **S. Idlahcen** – Experimental Setup, Investigation (Supporting); **A. Cessou** – Original Raman Setup and Raman Software Development, Fundraising, Project Management, Validation, Supervision, Writing – Review & Editing; **D. Honoré** – Fundraising, Project Management, Validation, Supervision, Writing – Review & Editing; **B. Lecordier** – Raman Software Development, Validation, Supervision, Writing – Review & Editing.

Declaration of competing interest

The authors declare that they have no known competing financial interests or personal relationships that could have appeared to influence the work reported in this paper.

Acknowledgments

This research work was supported by the Normandie Regional Council and the EU's European Regional Development Fund (ERDF) in the framework of the RAPHYD project (RIN 2018). A. Mahuthannan's stay at the CORIA laboratory was sponsored by the Research Council of Norway (grant number 268369).

Supplementary materials

Supplementary material associated with this article can be found, in the online version, at doi:10.1016/j.proci.2024.105708.

References

[1] T. Capurso, M. Stefanizzi, M. Torresi, S.M. Camporeale, Perspective of the role of hydrogen in the 21st century energy transition, Energy Convers. Manag. 251 (2022) 114898.
[2] H. Levinsky, Why can't we just burn hydrogen? Challenges when changing fuels in an existing infrastructure, Prog. Energy Combust. Sci. 84 (2021) 100907.
[3] K. Rajamanickam, F. Lefebvre, C. Gobin, G. Godard, C. Lacour, B. Lecordier, A. Cessou, D. Honoré, Effect of H2 addition on the local extinction, flame structure, and flow field hydrodynamics in non-premixed bluff body stabilized flames, Phys. Fluids 35 (2023) 047110.
[4] F. Guichard, P. Boubert, D. Honoré, A. Cessou, CO2 Spontaneous Raman Scattering: an alternative thermometry for turbulent reactive flows, in: 19th Int. Symp. Appl. Laser Imaging Tech. Fluid Mech., 2018, pp. 16–19.
[5] H. Ajrouche, A. Lo, P. Vervisch, A. Cessou, Assessment of a fast electro-optical shutter for 1D spontaneous Raman scattering in flames, Meas. Sci. Technol. 26 (2015) 075501.
[6] W. Coenen, L. Lesshafft, X. Garnaud, A. Sevilla, Global instability of low-density jets, J. Fluid Mech. 820 (2017) 187–207.
[7] Y. Zhu, V. Gupta, L.K. Li, Onset of global instability in low-density jets, J. Fluid Mech. 828 (2017) R1.
[8] B.B. Dally, A.R. Masri, R.S. Barlow, G.J. Fiechtner, Instantaneous and mean compositional structure of bluff-body stabilized nonpremixed flames, Combust. Flame 114 (1998) 119–148.
[9] Y. Chen, C. Chang, K.L. Pan, J.T. Yang, Flame lift-off and stabilization mechanisms of nonpremixed jet flames on a bluff-body burner, Combust. Flame 115 (1998) 51–65.
[10] H. Yamashita, M. Shimada, T. Takeno, A numerical study on flame stability at the transition point of jet diffusion flames, in: Symp. Int. Combust., Elsevier, 1996, pp. 27–34.
[11] A.M. Briones, S.K. Aggarwal, V.R. Katta, A numerical investigation of flame lift-off, stabilization, and blowout, Phys. Fluids 18 (2006).
[12] S. Hartl, D. Geyer, A. Dreizler, G. Magnotti, R.S. Barlow, C. Hasse, Regime identification from Raman/Rayleigh line measurements in partially premixed flames, Combust. Flame 189 (2018) 126–141.
[13] K. Wan, S. Hartl, L. Vervisch, P. Domingo, R.S. Barlow, C. Hasse, Combustion regime identification from machine learning trained by Raman/Rayleigh line measurements, Combust. Flame 219 (2020) 268–274.